Investigation of hetero-phases grown via in-situ exsolution on a Ni-doped (La,Sr)FeO$_3$ cathode and the resultant activity enhancement in CO$_2$ reduction

Dhruba J. Deka [a], Jaesung Kim [a], Seval Gunduz [a], Mimoun Aouine [b], Jean-Marc M. Millet [b], Anne C. Co [c], Umit S. Ozkan [a],*

[a] *William G. Lowrie Department of Chemical and Biomolecular Engineering, The Ohio State University, Columbus, OH, 43210, United States*
[b] *Institut de Recherche sur la Catalyse et l'Environnement de Lyon, UMR 5256 Université Claude-Bernard Lyon 1, 69626, Villeurbanne Cedex, France*
[c] *Department of Chemistry and Biochemistry, The Ohio State University, Columbus, OH, 43210, United States*

A R T I C L E   I N F O

A B S T R A C T

Exsolution of metal nanoparticles from a perovskite oxide combined with concomitant oxygen vacancy creation can enhance the catalytic activity of the parent perovskite. In this study, a Ni-doped (La,Sr)FeO$_3$ perovskite was subjected to a controlled reduction environment for populating its surface with B-site metal nanoparticles and oxygen vacancies, which also led to the evolution of a Ruddlesden-Popper (RP) oxide phase. Environmental TEM and in-situ XRD showed that the metal nanoparticles started forming at temperatures as low as 400 °C and were firmly pinned to their position inside a perovskite socket, giving them high thermal stability and allowing the usage of such active materials as cathodes for high-temperature CO$_2$ reduction in solid oxide electrolysis cells. Electrocatalytic activity of the cathode for CO$_2$ reduction was improved following exsolution, wherein the enhancement brought about by the nanoparticles and oxygen vacancies was much greater than that caused by the evolved RP phase.

1. Introduction

Perovskite oxides (ABO$_3$, A = Alkali metal, B = Transition metal) are an important class of catalytic materials with highly versatile electronic structure and functional properties with applications in a range of energy and environment-related catalytic systems such as emission control, partial and complete oxidation of hydrocarbons, hydrogen production, fuel cells, electrolysis cells and solar cells [1]. There are many metal ions that can accommodate either the A-site or the B-site, and hence a large number of structurally stable perovskite oxides can be formed. Such a wide gamut of the compositional possibility of perovskites is what makes them useful in so many applications. The catalytic activity of a perovskite can be greatly enhanced by tuning the surface concentration of the B-site [2,3].

Recent studies show that the availability of the B-site metal on the perovskite surface can be increased by subjecting the material to a controlled reducing environment at high temperatures. Under such environments, highly reducible B-site metals such as Ni, Co, Fe migrate from the bulk to the surface and form stable metallic nanoparticles, a

process termed as 'redox exsolution' or 'solid-state recrystallization' or 'intelligent self-regeneration' depending on whether it is carried out in a reversible or irreversible manner [3–18]. While physical deposition techniques such as vapor deposition and chemical impregnation have limited control over the nanoparticle dispersion and size distribution, and often produce nanoparticles weakly bound to the support [19–21], the exsolution process leads to a controlled formation of metallic nanoparticles with a uniform distribution that are anchored to the parent perovskite surface. Such anchorage can provide excellent mechanical and thermal stability to these particles [4,19]. Exsolution process has also been shown to be reversible under redox conditions [7, 22], which creates a possibility of growing the catalytically active particles when they are needed and dissolve them back into the perovskite structure when the purpose is served. Moreover, exsolution can also occur under vacuum and applied electrical potential, instead of a reducing gas, which brings flexibility in the synthesis methods of these nanoparticles [11,23]. Even though higher activity and stability brought about by the reversible exsolution of noble metals from a perovskite host was reported more than a decade ago in the field of automotive

---

emissions control [24,25], it was the area of solid oxide fuel cells where the concept of exsolution found immense attention. While Barnet's group was one of the first to use this concept for solid oxide fuel cell electrodes [26], Irvine and his co-workers performed extensive investigations into the exsolution process and showed the formation of various transition metal nanoparticles from non-stoichiometric perovskites under a reducing environment and also under applied potential in a solid oxide electrolyte cell [5,19,22,23]. While a major portion of the studies were done on the exsolution of Ni/Fe/Co nanoparticles on doped strontium titanate perovskites [4,5,11,16,18,19,27–29], there have been a few investigations into other perovskite systems such as Ni-doped $(La,Sr)_{1-x}CrO_3$ [6,30], $La_{0.3}Sr_{0.7}Cr_{0.3}Fe_{0.6}Co_{0.1}O_{3-\delta}$ [31], $(La_{0.75}Sr_{0.25})$ $(Cr_{0.5}Fe_{0.35}Ni_{0.15})O_3$ [22], $La_{0.9}Mn_{0.8}Ni_{0.2}O_3$ [32], as well as double perovskite materials such as Co-doped $Pr_{0.5}Ba_{0.5}MnO_x$ [17] and Ni-doped $Sr_2Fe_{1.5}Mo_{0.5}O_6$ [33,34].

The immense potential of functional perovskites decorated with metallic nanoparticles has encouraged several investigations looking into their size, number density, structure and composition. While most of the characterization studies were performed ex-situ, there exists a few in-situ investigations. For example, in a recent work, Neagu and his co-workers investigated the growth epitaxy and formation kinetics of Ni nanoparticles from $La_{0.43}Ca_{0.37}Ni_{0.06}Tu_{0.94}O_3$ and $La_{0.8}Ce_{0.1}Ni_{0.4}Ti_{0.6}O_3$ perovskites using an environmental TEM [4]. Jo et al. also scrutinized the kinetics and energetics for formation of Co nanoparticles from $SrTi_{0.75}Co_{0.25}O_3$ perovskite host using in-situ TEM and density functional theory [11]. There are multiple advantages with in-situ characterization over its ex-situ counterpart. For example, adsorption of impurities and reoxidation of the exsoluted nanoparticles might occur when the sample is exposed to the environment after synthesis. Cooling down the sample after nanoparticle growth may also affect the crystal structure, size, and shape of the particles. Therefore, in-situ characterization of the exsolution process is of primary focus of the current study.

The majority of the perovskite oxides used to study the exsolution process are doped strontium titanates which have cubic symmetry with fairy well-defined surface atomic arrangements which makes observation of the nanoparticles and its interaction with the perovskite surface easier. However, when the perovskite structure is more distorted, e.g., in the case of lanthanum strontium ferrite that can change its crystal structure to orthorhombic, rhombohedral, tetragonal or cubic depending on the synthesis method, dopants and temperature [35,36], the exsolution process may cause additional structural modifications to the perovskite surface and make the study more difficult. Such hetero-phases other than the metal nanoparticles can have added effect over the catalytic performance of the materials, and surprisingly, this issue has not been addressed yet in the literature. In our earlier publications, we have reported an A-site deficient $La_{0.7}Sr_{0.2}FeO_3$ perovskite with Ni and Co as dopants at the B-site that showed high activity for co-electrolysis of H_2O and CO_2 to produce synthesis gas $(H_2 + CO)$ with controllable H_2/CO ratio [36–38]. A subsequent publication also showed that the Ni-doped variant $La_{0.7}Sr_{0.2}Ni_{0.2}Fe_{0.8}O_3$ (LSNF) has a much higher activity for hydrogen production from H_2O electrolysis with lower cell voltage and impedance than the $La_{0.7}Sr_{0.2}FeO_3$ cathode [39]. Ex-situ XRD performed on the post-electrolysis cathodes showed that secondary phases such as a Ruddlesden-Popper (RP) oxide and metallic Ni forms on the cathode during electrolysis, which caused the observed improvement in activity.

In the current paper, a detailed examination of these secondary phases using in-situ techniques such as in-situ XRD and environmental transmission electron microscopy (ETEM) is discussed. Dynamic exsolution of Ni nanoparticles under a reducing environment was observed as a function of temperature and the formation of the RP phase was found to accompany this process. The perovskite structure around the exsoluted particles was also seen to transform to accommodate the nanoparticles better and provide them with enhanced stability. The hetero-phase material containing the parent ferrite perovskite, RP phase and metallic nanoparticles was used as a cathode for CO_2 electrolysis in

a solid oxide electrolysis cell. A significantly higher CO_2 reduction activity was observed for the hybrid cathode as compared to the parent perovskite $La_{0.7}Sr_{0.2}Ni_{0.2}Fe_{0.8}O_3$ (LSNF) cathode. Besides, the effect of the hetero-phase on the electrochemical CO_2 reduction was addressed along with the characteristics of each phase examined using in-situ and ex-situ characterization.

2. Experimental section

2.1. Catalyst synthesis

$La_{0.7}Sr_{0.2}Ni_{0.2}Fe_{0.8}O_3$ perovskite oxide was synthesized using a citric acid-ethylenediaminetetraacetic acid complexation method. In this technique, a stoichiometric quantities of metal nitrate salts are dissolved in deionized water, adding EDTA (ethylenediaminetetraacetic acid) with a molar ratio of 1:1 to the total moles of metal ions. The temperature of the solution is set to 60 °C in a water bath and the pH is adjusted to 6 by dropping an ammonium hydroxide solution to dissolve the EDTA entirely. At this stage, citric acid and ethylene glycol are introduced to the solution. The solution is heated further to 90 °C, maintaining the pH at 6. When the solvent completely evaporates, the resulting sticky gel is dried at a temperature of 150 °C for 12 h and then calcinated to form a crystalline black powder of LSNF at a temperature of 1000 °C for 5 h.

2.2. Electrocatalytic activity test

Electrochemical CO_2 reduction was performed on a button cell composed of yttria-stabilized zirconia (YSZ) electrolyte, a $La_{0.85}Sr_{0.15}MnO_3$ (LSM)-YSZ (50 %–50 %) anode, and the cathodes under investigation. Details of the cell fabrication process can be found elsewhere [36,40]. In brief, YSZ green tape (ESL Electroscience Laboratory) with 125 microns of thickness densified at 1450 °C was screen-printed with a slurry of the synthesized cathode mixed with an ink vehicle (Nexceris) and sintered at 1300 °C. The LSM-YSZ (ESL Electroscience Laboratory) anode was printed on the other side of the disc with the same procedure, except for the sintering temperature at 1200 °C. The button cell was sealed onto an alumina tube using a glass seal (G018−354, Schott) with the anode side exposed to the atmosphere. With gold wires and gold paste as current collector, the cell was connected to a BioLogic potentiostat (SP-150) along with the current booster (VMP3) for electrochemical measurements. The electrochemical CO_2 reduction was carried out at 800 °C, flowing 10 ccm of 40 % of CO_2/He into the cathode side with the applied current densities of 0–7 mA/cm^2. A gas chromatograph (Shimadzu 2014) with a pulsed discharge ionization detector (PDHID) was used to quantify the exit gas from the cathode side. Each current density was applied for four hours to obtain steady state product analysis for a long duration. In general, the cell voltage changed gradually during the first one hour, while it remained constant (less than 3 % change) for the remaining three hours. The CO production rates were measured during this later three hours of steady state operation.

2.3. X-ray diffraction (XRD)

X-ray diffraction was conducted with the Bruker D8 Lead X-ray powder diffractometer using Cu Kα radiation (40 kV, 40 mA, 0.154 nm). An oven HTK1200 from Anton Paar was used to introduce the sample to air, He, or 5 % of H_2/N_2 for an ambient, an inert, or a reducing atmosphere, respectively. Ex-situ and in-situ X-ray diffraction data were collected from the sample with steps of 0.014° and duration of 0.75 s at temperatures ranging from 30 °C to 800 °C.

2.4. Transmission Electron Microscopy (TEM)

The in situ environmental transmission electron microscopy (ETEM) characterization of LSNF7228 sample was conducted using an FEI
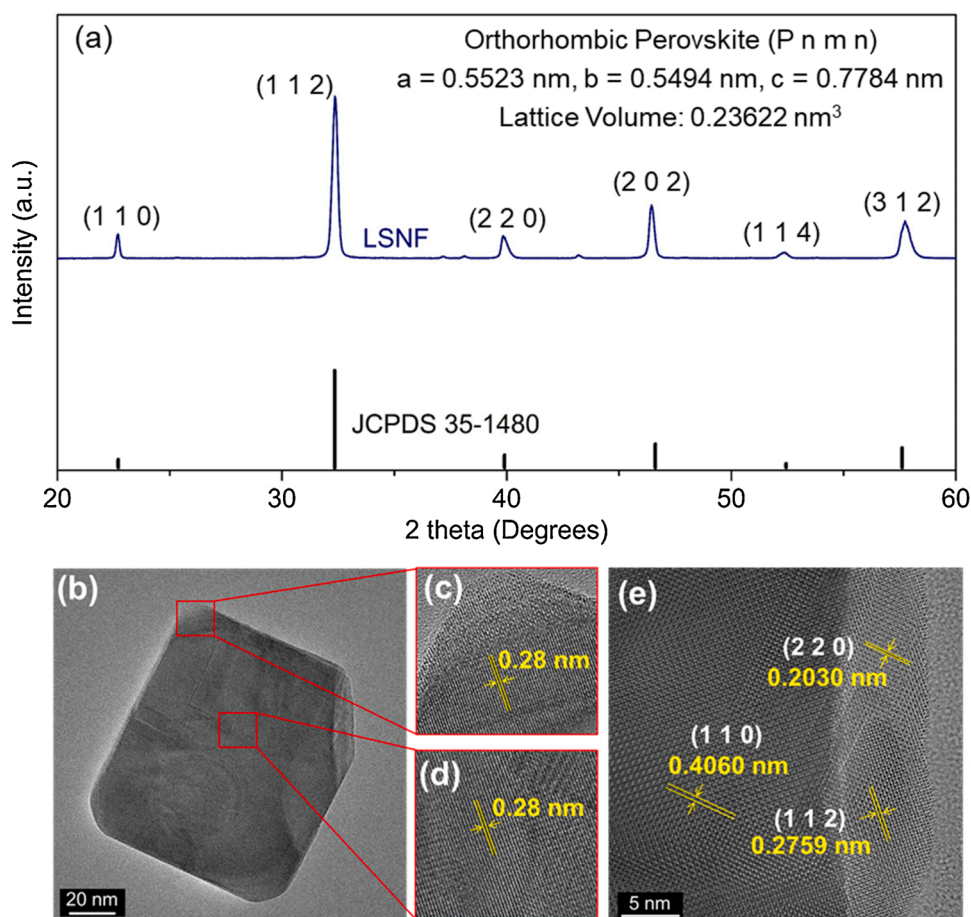
Fig. 1. (a) Room temperature XRD pattern of the as calcined LSNF and that of $La_{0.8}Sr_{0.2}FeO_3$ (JCPDS 35-1480), (b)-(d) TEM images of LSNF at room temperature with selected lattice fringes.

TITAN ETEM G2 80-300 kV instrument equipped with an objective C_s aberration corrector. The powdered sample was dispersed in ethanol using a sonicator. A drop of the suspension was dripped onto a carbon film supported on a copper grid placed in a Gatan furnace-type holder in Inconel for the direct observation of catalytic reactions at elevated temperatures and under a controlled atmosphere. Since the temperature was only measured with a thermocouple placed around the furnace of the sample holder, a slight discrepancy of few degrees may exist between the measured and real temperatures. The ETEM study has been conducted under vacuum or under hydrogen. In this last case, a home-made system of several Brooks mass flow controllers and a Valco two-position switching valve was used to maintain the pressure of H_2 to 1 mbarr. The presence of hydrogen was checked by continuously analyzing the effluent exiting the microscope chamber by mass spectroscopy (Pfeiffer). The samples were studied at 20 °C and between 400 and 800 °C. Energy dispersive spectra were collected ex-situ on LSNF sample treated under reducing environment at 800 °C for 2 h using an FEI Image Corrected Titan3 G2 60-300 STEM, which was a different instrument from the ETEM mentioned above.

2.5. Temperature-programmed oxygen evolution and temperature-programmed reduction

The evolution of oxygen from perovskite samples was studied to investigate oxygen vacancy formation at high temperatures. The signal for O_2 ($m/z = 32$) was scanned by a mass-spectroscope while heating a 50 mg sample of LSNF under a 30 ccm of He flow after a pretreatment under 10 % O_2/He at 1000 °C. The temperature-programmed reduction for the perovskite samples was also conducted by measuring a signal for

H_2O ($m/z = 18$) by flowing 30 ccm 5 % of H_2/N_2 after a pretreatment under 10 % O_2/He at 1000 °C.

2.6. Diffuse reflectance infrared Fourier transform spectroscopy (DRIFTS)

Temperature-programmed desorption of CO_2 using a DRIFTS setup was performed on the as-calcined LSNF, LSNF reduced for 2 h at 800 °C and La_2NiO_4. Samples diluted with KBr (1:20 ratio by weight) was loaded into a Praying Mantis DRIFTS cell which was placed inside a Thermoelectron Nicolet 6700 FTIR instrument containing an MCT detector. The sample was first pretreated at 450 °C under helium and cooled down to 50 °C. CO_2 was adsorbed at 50 °C for 1 h and was desorbed under helium flow as a function of temperature. IR spectra were collected during the temperature-programmed desorption process.

2.7. X-ray absorption near edge structure (XANES)

XANES experiments were performed at sector 10-BM of the Materials Research Collaborative Access Team (MRCAT) at the Advanced Photon Source (APS, Argonne National Laboratory). The samples were mixed with boron nitride in the weight ratio of 1:5, ground well, and then pressed into a sample holder containing cylindrical hole of 0.12 cm^2 cross-sectional area. The measurements were performed in transmission mode at Fe K-edge (7112 eV) and Ni K-edge (8333 eV). Each measurement on the samples was coupled with X-ray absorption spectra of the corresponding metal foil in order to calibrate the data for any shift in X-ray energy.
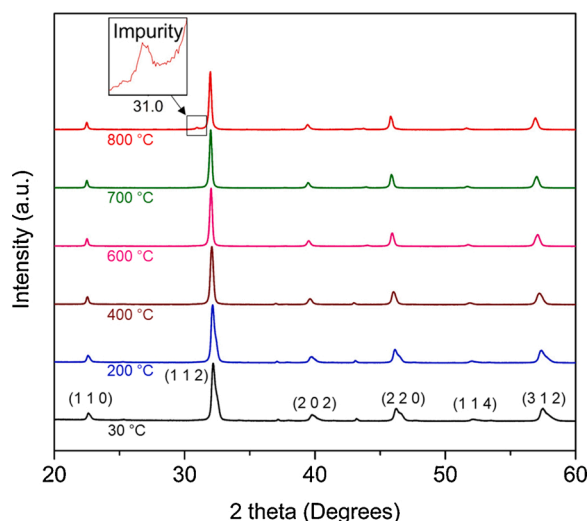
Fig. 2. In-situ XRD of LSNF under 5% H_2/N_2 at different temperatures.

Fig. 3. Room temperature XRD of LSNF, LSNF treated with 5% H_2/N_2 at 800 °C for 2 h, and La_2NiO_4 powder.

3. Results and discussion

3.1. Structural analysis of as-calcined LSNF

X-ray diffraction and transmission electron microscopy techniques were used to study the structure of the as-calcined LSNF powder sample. Fig. 1(a) shows its room-temperature XRD pattern. The positions of the diffraction peaks could be referenced to those of $La_{0.8}Sr_{0.2}FeO_3$ (JCPDS 35-1480), which is orthorhombic perovskite in structure. There are two minor peaks between 35°–40° and another one at 43°. NiO shows the (111) diffraction peak at 37° and (200) peak at 43°, which is the same range in which these minor additional peaks are seen. However, these peaks could also belong to (La,Sr)FeO$_3$ (JCPDS 35-1480, JCPDS 82-1959, JCPDS 82-1960), which does not have any Ni doping. Because of this ambiguity, and the fact that these peaks are small, we did not assign them to any specific phase. The unit cell volume calculated from the XRD pattern was 0.23622 nm^3, which is slightly lower than the lattice volume obtained for $La_{0.7}Sr_{0.2}FeO_3$ perovskite oxide in earlier studies. This decrease in the lattice volume is due to the replacement of Fe-ions by Ni-ions, which are smaller in size (ionic radii values). The LSNF sample is polycrystalline in nature with an average crystallite size of 35 nm as calculated using the Scherrer equation.

The room-temperature TEM images of LSNF shown in Fig. 1(b)–(e) reiterates the observations made from XRD. Fig. 1(b) shows the TEM image of an LSNF particle and magnified images of the regions marked in red squares are shown in Fig. 1(c) and (d). A d-spacing of 0.28 nm is observed in these two figures, which is close to the d-spacing of the (1 1 2) plane. Fig. 1(e) shows a higher resolution image showing that lattice fringes in greater detail. d-spacing corresponding to (2 2 0), (1 1 2), and (1 1 0) planes could be identified indicating that sample is polycrystalline.

3.2. Structural analysis of LSNF treated under reducing environment

In-situ XRD patterns of LSNF under 5% H_2/N_2 in the temperature range of 30°–800 °C are shown in Fig. 2, whereas those under air and helium environments are shown in Figure S1 (a) and (b) in the Supplementary Information section. XRD under air and helium at all temperatures shows the presence of only the perovskite phase. The diffraction peaks shift to lower 2-theta values as the temperature is increased because of thermally induced lattice expansion. When the environment is switched to 5% H_2/N_2, additional impurity peaks starts appearing at 800 °C, as seen in the inset in Fig. 2. This indicates that even though the perovskite phase is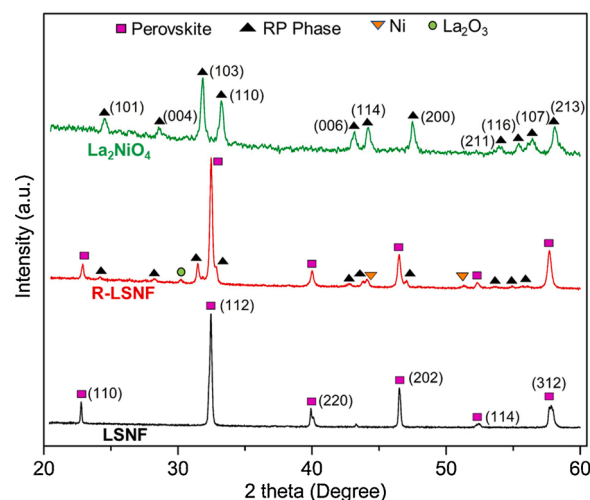 stable under oxidizing or inert environment, secondary phases start forming at high temperatures under a reducing environment.

To understand the nature of such secondary phases, LSNF powder was treated with 5% H_2/N_2 at 800 °C for 2 h and it's XRD pattern was collected. Fig. 3 shows the XRD patterns of as-calcined LSNF, reduced LSNF and La_2NiO_4. The reduced LSNF was seen to contain the perovskite structure as the primary phase, with a La_2NiO_4- type phase and metallic nickel as the secondary phases. Raman spectra shown in Fig. S2 shows that the spectrum of reduced LSNF contains contributions from LSNF and La_2NiO_4, e.g., ~144 cm^{-1} band in common with the perovskite phase and ~216 cm^{-1} band in common with the La_2NiO_4 phase, which agrees well with the XRD data.

La_2NiO_4 is a mixed electronic and ionic conductor containing a perovskite-like crystal structure called the Ruddlesden-Popper (RP) phase. The general chemical formula of RP oxides is $A_{m+1}B_mO_{3m+1}$ (m = 1, 2, 3 and so on) where A is an alkali, alkaline earth or rare earth metal while B is a transition metal. The structure of these oxides consists of 'm' numbers of perovskite (ABO$_3$) layers separated by a rock-salt type AO layer. When m = 1, the chemical formula is A_2BO_4, and La_2NiO_4 falls in this category. When m = ∞, the structure becomes a perovskite oxide. Due to the presence of oxygen hyperstoichiometry, RP phase oxides may have better oxide ion conductivity than the corresponding perovskites which has prompted an increased attention on such oxides for application as a potential anode catalyst in solid oxide fuel cells.

One can notice that XRD peaks corresponding to the RP phase observed in the diffractogram of reduced LSNF sample appear at slightly lower 2-theta values than that observed in the diffractogram of La_2NiO_4. This is explained by the fact that LSNF has two B-site metals: Fe^{3+} as the main ion and Ni^{3+} as the dopant. This leads to the incorporation of both Ni and Fe into the B-site of the secondary RP phase formed upon the reduction of LSNF. Since Fe ions have bigger ionic radii than Ni ions, that makes the unit cell volume to increase, thereby shifting the diffraction lines to shift to lower 2-theta. With a similar argument, it can also be said that the metallic nickel phase formed on LSNF will also contain Fe to form an alloy. Diffraction lines for both Ni and Ni-Fe alloys appear at similar 2-theta values, and therefore it is difficult to arrive at a conclusion regarding the composition of such alloys based on XRD alone. In a later section, we will try to look at such composition in greater details using energy dispersive spectroscopy. For now, we will assume this phase as just metallic nickel for the ease of analysis and discussion.

The formation of the RP phase and the metallic nickel phase is by no means two independent events. In fact, the appearance of one phase is needed for the occurrence of the other under the reducing environment
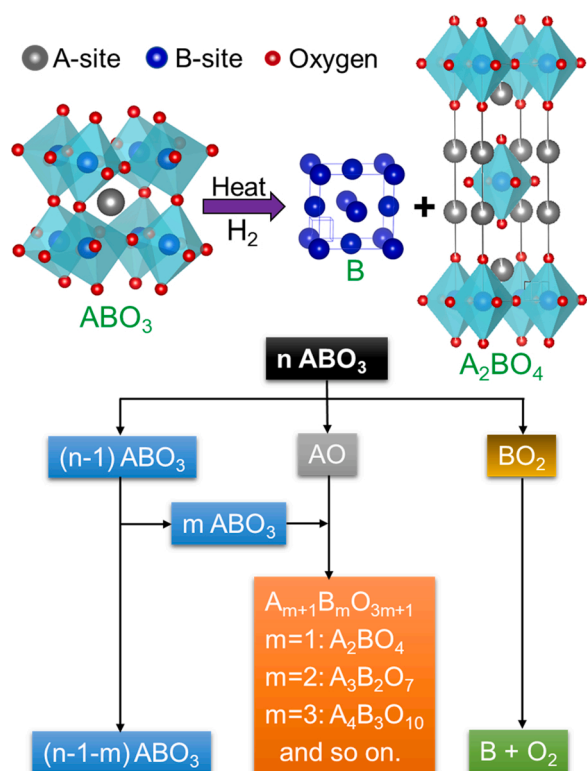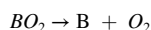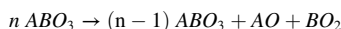
Fig. 4. Illustration of the simultaneous formation of B-site metal phase and a Ruddlesden- Popper phase during the exsolution process.

used here, and the underlying phase transformation steps can be proposed as follows:

$$n\ ABO_3 \rightarrow (n-1)\ ABO_3 + AO + BO_2$$

$$BO_2 \rightarrow B\ +\ O_2$$

$$ABO_3\ +\ AO \rightarrow A_2BO_4$$

This phase evolution process is also illustrated schematically in Fig. 4. An ABO_3 formula unit can break down into individual oxides of A- and B-site metals, i.e., AO and BO_2, respectively. BO_2 reacts with H_2 to produce metallic B and oxygen vacancies. On the other hand, AO can combine with one (m = 1) or more (m = 2, 3, and so on) ABO_3 formula units to form A_2BO_4 or higher-order RP phase oxides. Therefore, in summary, the partial reduction of the perovskite oxide can lead to the formation of (i) a B-site metal phase, (ii) an RP oxide phase and (iii) oxygen vacancies, thereby altering the structural and catalytic properties of the parent perovskite.

XRD is a bulk technique meaning that changes occurring to the surface of the sample may not be detected, as the majority of the signal comes from the bulk structure. Considering the fact that in-situ XRD detects the formation of an additional phase at 800 °C under reducing environment, which was later confirmed as an RP phase and a B-site metal phase by ex-situ XRD performed on the sample treated with 5 % H_2/N_2 at 800 °C for 2 h, there is a possibility that the onset of such phase formation can occur at a lower temperature but not be detectable by XRD. With this hypothesis in mind, environmental transmission electron microscopy (ETEM) experiments were carried out on LSNF under hydrogen (1 mbar) as a function of temperature in the range of 25 °C – 800 °C.

The ETEM image of LSNF at room-temperature was already discussed in Fig. 1, which confirms that the sample is a polycrystalline perovskite oxide. No additional features were observed up to 400 °C, beyond which the formation of metallic nanoparticles were detected. Fig. 5(a), (b) and (c) shows the ETEM images collected at 400 °C, 450 °C and 500 °C, respectively. Although the signal is low, the appearance of a nanoparticle of approximately 2 nm x 1 nm is confirmed on the surface of the perovskite at 400 °C, as marked by the red square in Fig. 5(a). Inverse fast Fourier Transform (IFFT) was attempted on the region inside this square and shown as an inset in Fig. 5(a). Due to the low signal, only one lattice distance of approximately 0.229 nm could be evidenced, which is close to the value for (1 1 1) or (1 1−1) plane of nickel (0.2035 nm). The signal from the nanoparticle improves as the temperature increase to 450 °C and 500 °C. The respective IFFT also becomes sharper, and the lattice distances are calculated to be 0.217 and 0.207 nm, respectively, which agree well with the lattice distance of Ni (1 1−1). Details of such indexing are shown in Table S1 in the supplementary section.

As mentioned above, XRD is able to detect this metallic phase only after reduction at 800 °C. However, ETEM results show the formation of the metallic phase as nanoparticles starting at 400 °C. To our knowledge, this is the lowest temperature reported yet at which exsolution of metallic nanoparticles has been observed. Ability to exsolve nanoparticles at low temperature can have potential applications in many catalytic reactions, including but not limited to automotive emission control catalysis, PEM fuel cells, photocatalysis, hydrocarbon reforming. The operating temperature in these applications can be as low as room temperature. Moreover, with the advent of new highly conducting electrolytes for solid oxide fuel cells, it has been possible to reduce their operating temperatures below 500 °C with appreciable performance. Therefore, it is important to know the temperature dependance of the exsolution phenomenon, so that some light can be shed into whether in-situ exsolution can be a viable option in these applications. Also, knowing the temperature dependence of the exsolution process will help in finding the required temperature for a desired size distribution of the nanoparticles, and thereby can enable catalyst synthesis strategies for targeted applications. It, therefore, is important to probe the nanoparticle formation in-situ for detecting the temperature at which the process initiates. However, there are not many studies in the literature
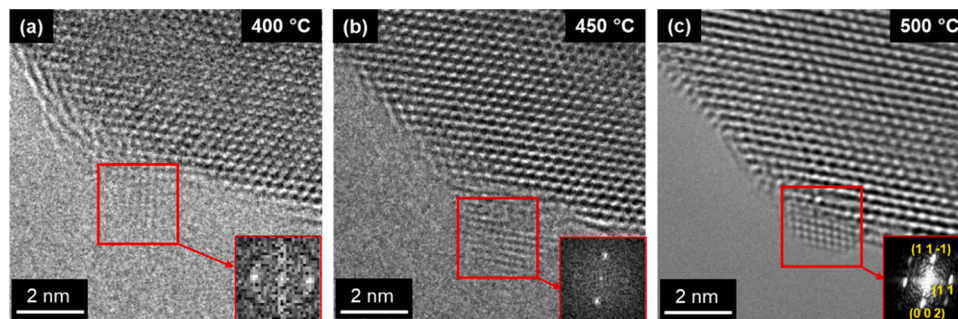

Fig. 5. In-situ TEM of LSNF under 5 % H_2/N_2 collected at (a) 400 °C, (b) 450 °C and (c) 500 °C with fast Fourier transform of selected areas, showing growth of Ni nanoparticles.
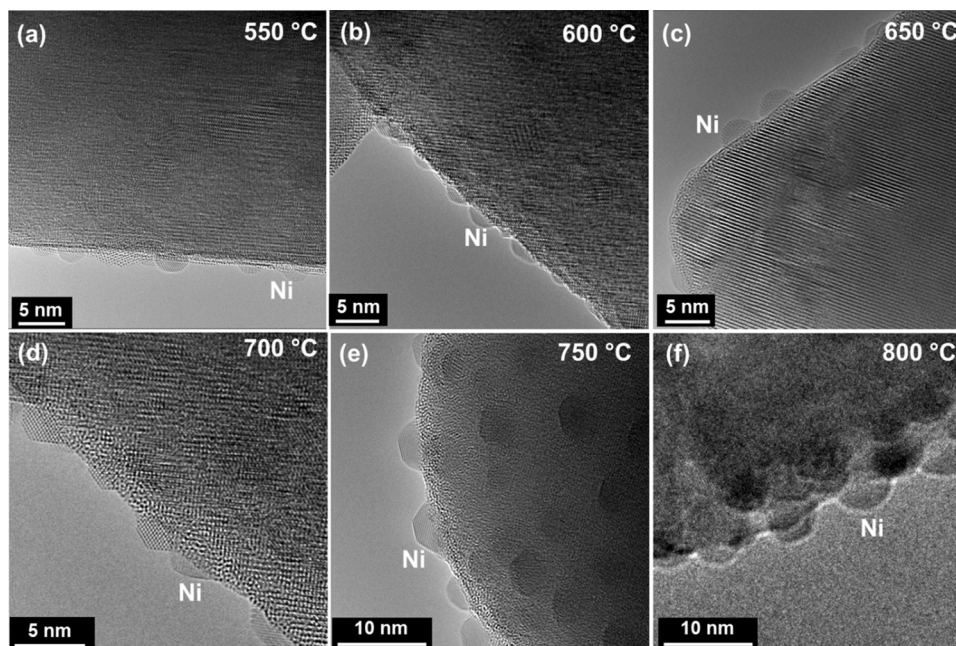
Fig. 6. In-situ TEM of LSNF under 5 % H_2/N_2 collected at (a) 550 °C, (b) 600 °C, (c) 650 °C, (d) 700 °C, (e) 750 °C, and (f) 800 °C.
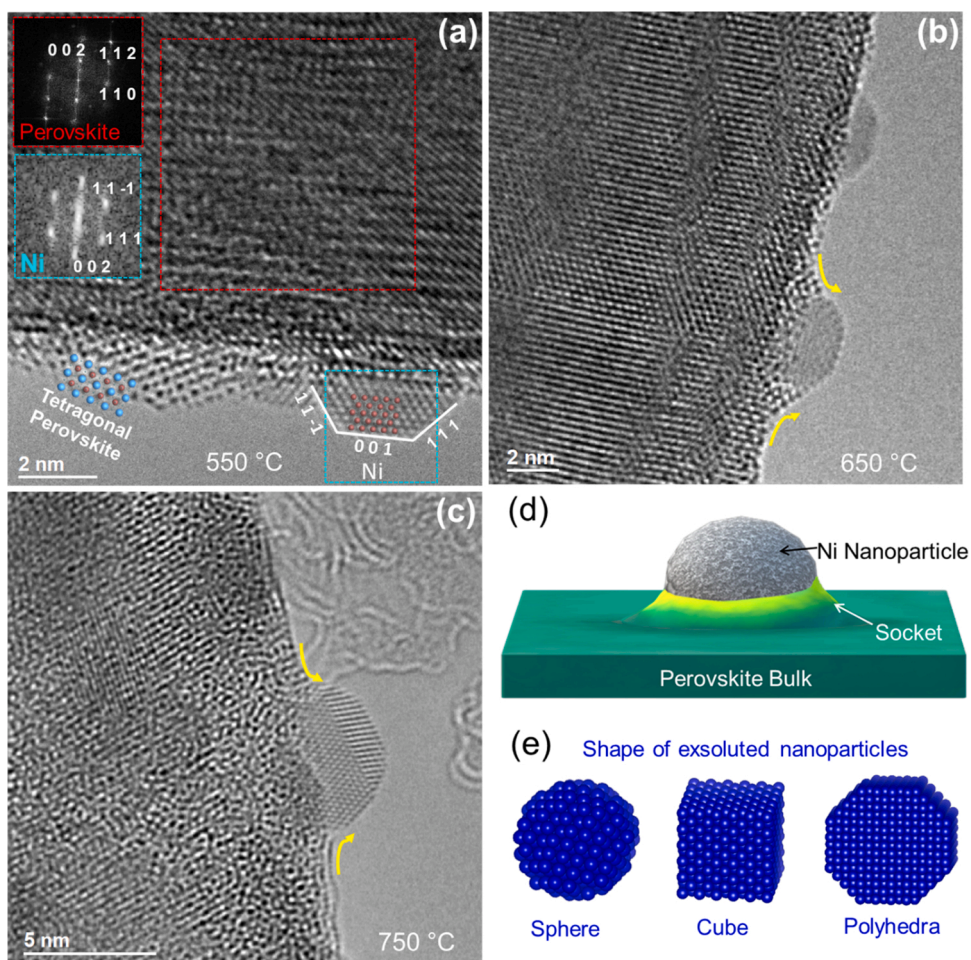

Fig. 7. In-situ TEM of LSNF under 5 % H_2/N_2 collected at (a) 550 °C, (b) 650 °C, (c) 750 °C showing formation of a socket around the nanoparticle. (d) a schematic illustration of socket formation around a nanoparticle, (e) a schematic illustration of various shapes observed for the nanoparticles.
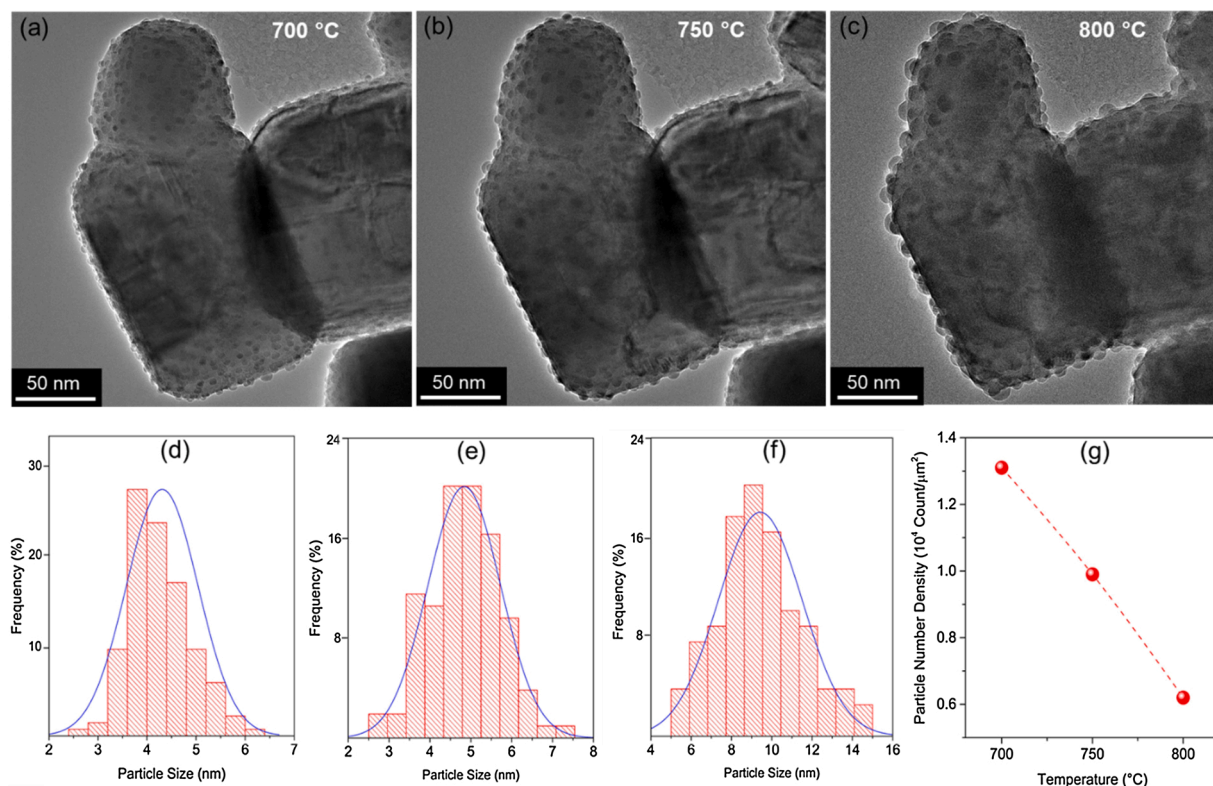
Fig. 8. In-situ TEM of LSNF under 5 % H_2/N_2 collected at (a) 700 °C, (b) 750 °C and (c) 800 °C showing formation of nanoparticles, (d)-(f) show distribution of particle sizes at these three temperatures, (g) nanoparticle number density at these three temperatures.

that have characterized the exsolution process in-situ as a function of temperature. In a recent paper, Jo et al. investigated the formation of cobalt nanoparticles on a $SrTi_{0.75}Co_{0.25}O_{3-\delta}$ parent perovskite under high vacuum using in-situ TEM. Exsolution of nanoparticles was observed at 500 °C in this study [11]. Sun et al. investigated the formation of cobalt nanoparticles on a Co-doped $Pr_{0.5}Ba_{0.5}MnO_x$ double perovskite oxide using ETEM technique and observed the onset of the exsolution process at 810 °C [17]. However, the resolution of the images reported in this study was not very high, which brings the question of whether the nanoparticles indeed started forming at a lower temperature, but could not be detected due to low resolution. Another study that used the in-situ TEM technique was done by Neagu et al., where temporal evolution of nickel nanoparticles from parent perovskites $La_{0.43}Ca_{0.37}Ni_{0.06}Ti_{0.94}O_3$ and $La_{0.8}Ce_{0.1}Ni_{0.4}Ti_{0.6}O_3$ was studied at constant temperatures of 650 °C and 900 °C [4]. There are many more studies that investigate the exsolution process by first treating the perovskite at high temperature in a reducing environment and then characterizing the sample by techniques such as SEM, TEM and AFM. For example, Kwon et al. reported the formation of nickel and cobalt nanoparticles on $PrBaMn_{1.7}Co_{0.3}O_{5+\delta}$ and $PrBaMn_{1.7}Ni_{0.3}O_{5+\delta}$ parent perovskites when reduced at 800 °C [14]. Exsolution of nickel nanoparticles was observed to take place from a $SrFe_{0.85}Ti_{0.1}Ni_{0.05}O_{3-\delta}$ perovskite when treated at 600 °C as reported by Yang et al. [41], however a long reduction duration of 40 h was used in this study. Such a long reduction time is mainly caused by the slow kinetics of exsolution which renders these kind of perovskite systems not suitable for in-situ studies.

Continuing with the discussion on ETEM results, Fig. 6(a)–(f) show the images of the perovskite at 50 °C intervals in the range of 550 °C – 800 °C. Nickel nanoparticles are observed at all these temperatures. The average size of the nanoparticles seems to stay constant at around 5 nm at temperatures up to 700 °C but increases at 750 °C and 800 °C. Even though an attempt was made to capture the temporal growth of a particle at specific temperatures, it did not bring much success as there were

long periods of time without any particle formation followed by the sudden appearance of several particles simultaneously. Such an observation can be explained by the mechanism of exsolution. On exerting a perovskite to a reducing environment, oxygen vacancies first start forming and when the concentration of such vacancies reaches a limiting level, the surface of the perovskite becomes destabilized and leads to the diffusion of the B-site ion towards the surface for stabilizing the structure [5,19,42]. During this first step of the exsolution process, particles are not yet formed on the surface which explains the observed initial period when no particles were seen. The transported B-site ions then get reduced on the surface, assemble and initiate the formation of nanoparticles. However, this second step was fast enough that it could not be captured as a function of time and led to the observed sudden appearance of nanoparticles.

Fig. 7(a)–(c) shows the perovskite with a Ni particle at three different temperatures revealing that the surface of the perovskite near the nanoparticle changes its crystal structure as compared to the bulk. It was possible from Fig. 7(a) to identify this modified surface layer to consist of a tetragonal perovskite structure. Because of the presence of such an intermediate layer, it is difficult to determine a definite epitaxial relationship between the parent perovskite and the Ni particle. While the Ni particle was seen to grow along the (0 0 1) plane in Fig. 7(a), the exact orientation of the perovskite crystal could not be assessed at the interface with the nanoparticle due to its modified crystal structure. This crystallographic orientation of the nanoparticle is similar to that observed by Neague and coworkers during the exsolution of Ni nanopartcles from a $La_{0.43}Ca_{0.37}Ni_{0.06}Ti_{0.94}O_3$ perovskite [4]. However, this was not the only epitaxy possible for the Ni nanoparticles, as growth along the (1 1 −1) plane was also observed in Fig. 5 (c). Moreover, even though the exact orientation of the perovskite crystal could not be determined at the interface, it is obvious that the crystallographic orientation of the perovskite along with the growth of the nanoparticles is not the same in Figs. 5(c) and 7 (a). Therefore, while the diffusion of ions in the highly symmetric structure of the cubic perovskites such as
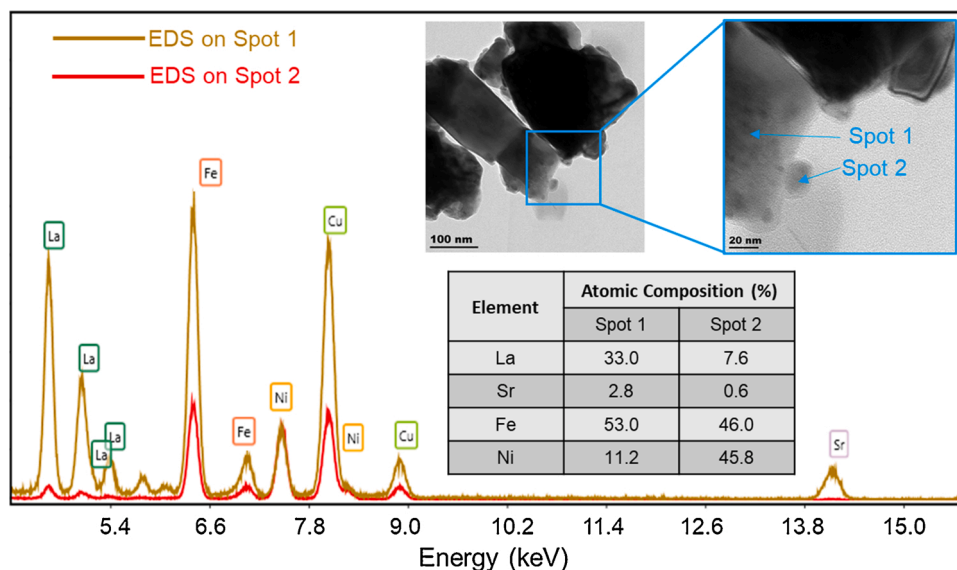
Fig. 9. Energy dispersive spectra of LSNF treated under 5 % H_2/N_2 at 800 °C for 2 h collected at two different spots. Spot 1 was from the perovskite structure near to a nanoparticle and spot 2 was from the nanoparticle.

the doped strontium titanates primarily takes place along the (1 1 0) orientation as reported in the literature [4,19], current observations show that a more isotropic diffusion takes place in an orthorhombic or tetragonal perovskite such as doped lanthanum ferrites. This is most likely due to their relatively distorted structure, which leads to the formation of nanoparticles in more than one crystallographic orientation.

The tetragonal perovskite phase was observed to form a volcano-like elevated structure around the nanoparticle, as shown in Fig. 7(b) and (c). Such a volcano-like structure works as a socket leading to a strong anchoring of the nanoparticle into the perovskite support. A schematic illustration of the socketing phenomenon is shown in Fig. 7(d). Due to such socketing event, the in-situ exsolved nanoparticles tend to be highly stable and avoid sintering at higher temperatures as compared to nanoparticles formed by external deposition methods such as the impregnation process. Evidence of such a stabilization process is seen in Fig. S4 (as well as in Appendix AVideo 1 captured in real time) that shows a socketed nanoparticle at 650 °C that changes its shape laterally but is so well anchored to the perovskite via the tetragonal socket that it cannot migrate from its place. Such lateral shape changes make the Ni nanoparticles highly dynamic and that may have interesting implications when used as heterogeneous and electrochemical catalysts. As illustrated in Fig. 7(e), nanoparticles with various shapes such as a sphere, cube and polyhedral were observed in the current study. The ratio of the width of the nanoparticles to their height exposed above the perovskite surface was found to be between 2–3 for all the temperatures, which reveals that the exsolution process and particle growth is isotropic, irrespective of their shapes.

Figs. S5 and 8 show the ETEM images collected at 700 °C, 750 °C and 800 °C that includes a large number of nanoparticles, enabling us to perform analysis on the nanoparticle size distributions and number density as a function of temperature. On visual inspection of Fig. 8(a), (b) and (c) that shows the same region of the sample, it is obvious that the size of the nanoparticles increases marginally when the temperature is raised from 700 °C to 750 °C followed by a greater increase when heated to 800 °C. Similarly, the number of particles can be seen decreasing as the temperature is increased. Fig. 8(d), (e) and (f) show the distribution of particle size at 700 °C, 750 °C and 800 °C, respectively. More than 100 particles at each temperature were used to construct these statistics. The average nanoparticle size was found to be 4.5 nm and 4.8 nm at 700 °C and 750 °C, respectively, which increases to 9.5 nm

at 800 °C, indicating almost a step-change in the average particle size above 750 °C. Particles in the size range of 2 nm – 7 nm and 2 nm – 8 nm were observed at 700 °C and 750 °C, respectively. Even though the average sizes are similar at 700 °C and 750 °C, a higher fraction of particles were available in the range of 4 nm – 6 nm at 750 °C than at 700 °C. The distribution of the particle size was much wider at 800 °C as particles with sizes ranging from 4 nm to 15 nm were formed. The size range so observed is similar to that reported for Ni nanoparticles on doped strontium titanate perovskite, and is much smaller than the 25–60 nm range reported for the Ni-doped $Sr_2Fe_{1.5}MoO_6$ double perovskite system [33,43,44]. Fig. 8(e) shows the number density of nanoparticles at 700 °C, 750 °C and 800 °C, which were calculated to be 1.31×10^4, 0.99×10^4 and 0.62×10^4 per μm^2, respectively. These number densities are more than 20 times higher than those obtained during the exsolution of Ni from a $La_{0.5}Ca_{0.4}Ni_{0.2}Ti_{0.8}O_{2.95}$ perovskite at the same temperatures [9], thereby indicating that a much higher nanoparticle count can be achieved on distorted perovskites such as ferrites compared to the highly symmetric cubic titanates. The increase in the average size and decrease in number density with increasing temperature can be due to two processes: (i) the continuing exsolution of the B-site atoms that gradually increases particle sizes and (ii) the agglomeration of two particles very close to each other as both grow during exsolution. The exsolution process has been shown to be a reactant limiting process [4, 42,45], meaning that the rate of nanoparticle growth reduces when the exsolvable atoms become diminished. As a result, the nanoparticles should not grow further once the limiting condition is achieved, which will solve the problem of increasing particle size and decreasing number density with higher temperatures. This observation was indeed made in the current study.

The discussion of ETEM images was based on Ni as the constituent of the metallic nanoparticles. For assessing the presence of Fe in these nanoparticles, ex-situ energy dispersive spectra (EDS) were collected from an LSNF sample treated with H_2/N_2 at 800 °C for 2 h. Such ex-situ measurements were taken because EDS could not be collected during the ETEM experiments. The instrument used for the EDS had a much lower resolution than the ETEM instrument, as evident from the images shown in Fig. 9. The EDS collected from two different spots on the sample are also shown in Fig. 9. Spot 1 was on the perovskite oxide and spot 2 was on a nanoparticle. The average composition of the two spots are tabulated inside Fig. 9. Spot 1 has a high contribution from La and Fe as lower contribution from Sr and Ni as expected from the perovskite
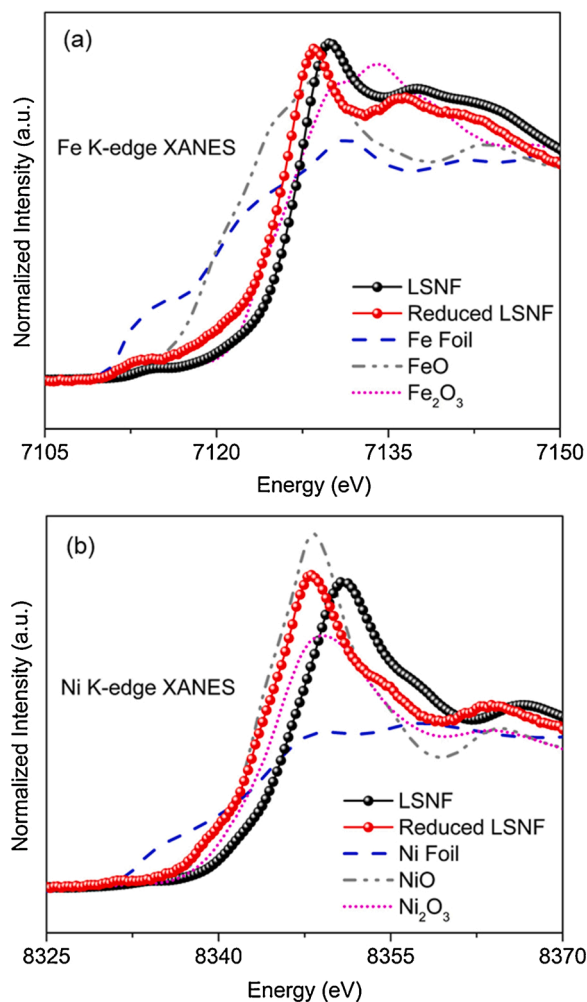
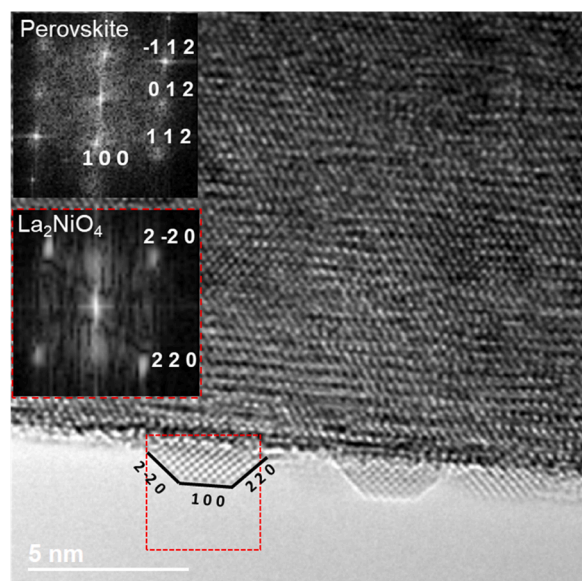**Fig. 10.** XANES of LSNF and reduced LSNF, (a) Fe K-edge, (b) Ni K-edge.

Fig. 11. In-situ TEM of LSNF under 5 % H_2/N_2 collected at 750 °C, showing formation of La_2NiO_4- type Ruddlesden- Popper phase on the surface of the parent perovskite (facetted nanoparticles). IFFT of the perovskite region and the RP phase region (marked in red square) are also shown as insets.
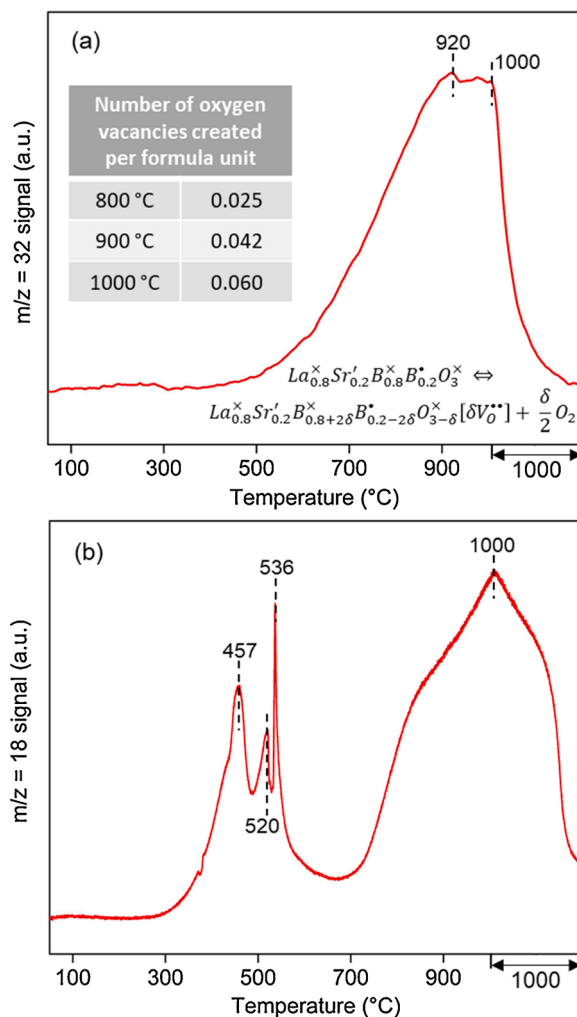

Fig. 12. (a) oxygen vacancy formation in as-calcined LSNF under helium environment, (b) temperature- programed reduction (TPR) profile of LSNF collected under 5 % H_2/N_2 flow.

phase. Contribution from La and Sr is very low at spot 2, meaning that it is on a B-site metal particle. The relative amount of Ni to Fe increases by five times from spot 1 to spot 2, which indicates that Ni is exsolved at a much higher degree than Fe. This is due to the reason that Gibb's free energy change associated with the reduction of Ni^{2+} to Ni is lower than that for the reduction of Fe^{3+} to Fe and Fe^{2+} to Fe from their oxides [6, 18,46].

The relative reducibility of the B-site ions in the perovskite structure was also investigated using XANES. Fig. 10 (a) and (b) show the ex-situ Fe K-edge and Ni K-edge XANES of LSNF and LSNF treated under 5 % H_2/N_2 at 800 °C for 2 h. XANES of the oxides of Fe and Ni as well as of Fe and Ni metal foils are also shown in these figures. The average oxidation state of Fe was found to be greater than 3+, which is typical in such Sr-doped lanthanum ferrite perovskites. However, upon reduction, the oxidation state of Fe changes marginally to 2.8 + . Similarly, in the case of Ni, the oxidation state before the reduction is greater than 3+, but becomes 2+ after reduction. Thus, Ni reduces to a greater extent compared to Fe, which is why it is exsolved more readily than Fe. In conclusion, the metal nanoparticles observed on the reduced LSNF are mainly composed of nickel but contains a fraction of iron, making them an alloy of Ni and Fe. Such alloy nanoparticles of Ni and Fe have also been reported to form by the reduction of Ni-doped $Sr_2Fe_{1.5}Mo_{0.5}O_6$ double perovskites [33,34,47].

The formation of B-site metal particles is accompanied by the evolution of an RP phase mixed metal oxide as already illustrated in Fig. 4

and experimentally observed from XRD. Fig. 11 shows a particle on the surface of the parent perovskite that could be assigned to La_2NiO_4. IFFT of this particle is also shown in the figure, which helps identifying the exposed planes of the particle as (1 0 0), (2−2 0) and (2 2 0) with the particle growing epitaxially along with (1 0 0) direction. However, it is possible that the RP phase is present also in some other form on the surface or beneath it in the parent perovskite, as the small number of nanoparticles of the phase observed in TEM cannot account for its high contribution to the XRD pattern of reduced LSNF shown earlier in Fig. 3. A Rietveld refinement of this pattern (Fig. S6) indicated the presence of approximately 17.9 wt% of the RP phase and 1.0 wt% of metal nanoparticles on the parent perovskite. Only a fraction of this RP phase is present as nanoparticles on the surface as already discussed. Since the metallic nanoparticles are mainly present as nanoparticles on the perovskite surface, it is expected that the metallic phase will have a greater influence on the catalytic properties of the material than the RP phase. This hypothesis was indeed found to be correct as discussed in sections 3.5 and 3.6.

3.3. Temperature-programmed oxygen evolution and temperature-programmed reduction

Fig. 12(a) shows the temperature-programmed evolution of oxygen from the as-calcined LSNF under helium flow. The process of oxygen vacancy creation by the release of oxygen atoms from the perovskite structure is illustrated using the Kröger-Vink notation inside Fig. 12(a). The formation of oxygen vacancies is an important property for electrode materials as these vacancies help in the conduction of oxide ions. Moreover, oxygen vacant sites also work as active sites during electrolysis of CO_2. As seen from Fig. 12(a), a small quantity of oxygen evolves below 300 °C. This type of oxygen is called the α-oxygen which consists of oxygen species adsorbed on the surface [36]. Above 500 °C, oxygen from the bulk perovskite structure starts evolving and the rate of such oxygen vacancy creation keeps on increasing till 920 °C, beyond which the rate becomes steady. This type of oxygen is called the β-oxygen. The β-oxygen signal was observed to decrease when the temperature was kept constant at 1000 °C. The number of oxygen vacant sites created per formula unit at 800 °C, 900 °C and 1000 °C is tabulated inside Fig. 12(a). The cumulative number of oxygen vacancies formed at 1000 °C was 0.060, which is not large enough to break down the perovskite structure but is sufficient enough to provide good ionic conductivity and electrochemical activity. A more detailed discussion of such oxygen vacancy creation was provided in an earlier publication [36].

Temperature- programmed reduction profile of LSNF under a flow of 5 % H_2/N_2 is shown in Fig. 12(b). The profile was created by monitoring the $m/z = 18$ signal, which comes from H_2O formed by the reaction between H_2 and O-atoms in the perovskite. Two different sets of reduction peaks are observed: one in between 300 °C and 700 °C and the other above 700 °C. The initial signal obtained between 300 °C–400 °C can mainly be assigned to the first step of the exsolution process which is the formation of oxygen vacancies. As the temperature rises, diffusion of the B-site ions to the surface, and their reduction takes place, as already discussed with ETEM results. The first set of peaks with maxima at 457 °C, 520 °C and 536 °C can, therefore, be assigned to the partial reduction of Fe^{3+} and Ni^{3+} ions to lower valent cations [30,48,49]. Some of these lower valent cations can be metallic as seen from ETEM results. This also agrees with the observation that the metallic nanoparticles were first seen at 400 °C. The formation of metallic Ni should be accompanied by the evolution of La_2NiO_4 as discussed with Fig. 4. Previously published studies on the TPR of $LaNiO_3$ perovskite suggest that the TPR peaks in this first set indeed contain contribution from the formation of the La_2NiO_4 phase [50,51]. The reduction of the B-site cations continues above 700 °C which leads to a large and wide reduction peak. This peak is a result of a complete reduction of B-site metal ions to the metallic phase, which leads to the formation of nanoparticles, as seen from ETEM
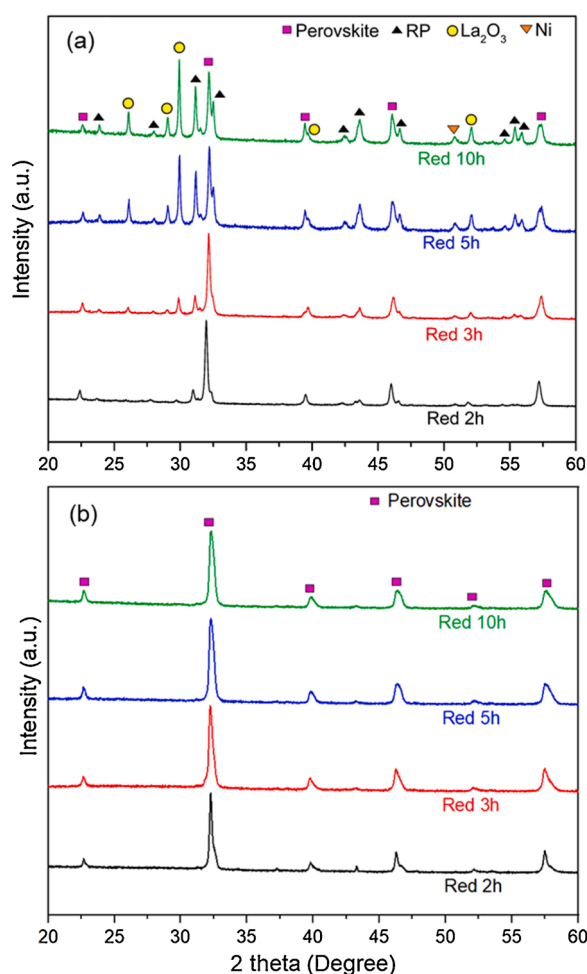

Fig. 13. (a) XRD of LSNF treated with 5 % H_2/N_2 at 800 °C for 2 h, 3 h, 5 h and 10 h, (b) XRD of each of the three samples after re-oxidation with 10 % O_2/He at 800 for 2 h.

results. The large, broad peak also contains a contribution from the formation of A-site or B-site metal oxides due to degradation of the perovskite structure at high temperatures, as confirmed by the XRD results below.

3.4. Redox reversibility of exsolved phases

Fig. 13(a) shows the room- temperature XRD patterns of LSNF samples reduced with 5 % H_2/N_2 at 800 °C for four different time durations: 2 h, 3 h, 5 h and 10 h. The diffractogram of the sample reduced for 2 h shows peaks of the perovskite, RP phase and metallic Ni. However, the La_2O_3 phase appears when the reduction time duration is 3 h, and the contribution of La_2O_3 increases as the reduction time is increased further. La_2O_3 is electronically non-conducting and therefore has a detrimental effect on the electrocatalytic performance of the cathode. Therefore, a reduction time of 2 h is optimum for creating metallic nanoparticles without causing the La_2O_3 phase to precipitate. Interestingly, the formation of all these secondary phases, including the undesired La_2O_3 phase, is completely reversible. The four LSNF samples reduced at four different time durations were re-oxidized under 10 % O_2/He and the XRD patterns of the re-oxidized samples are shown in Fig. 12(b). The diffraction peaks related to the secondary phases were not visible in these patterns, indicating that the exsolution process is highly reversible. Since the LSNF samples reduced for a longer duration of time undergoes complete reversal upon oxidation for 2 h, it can be inferred that the kinetics of oxidation and diffusion of the constituent
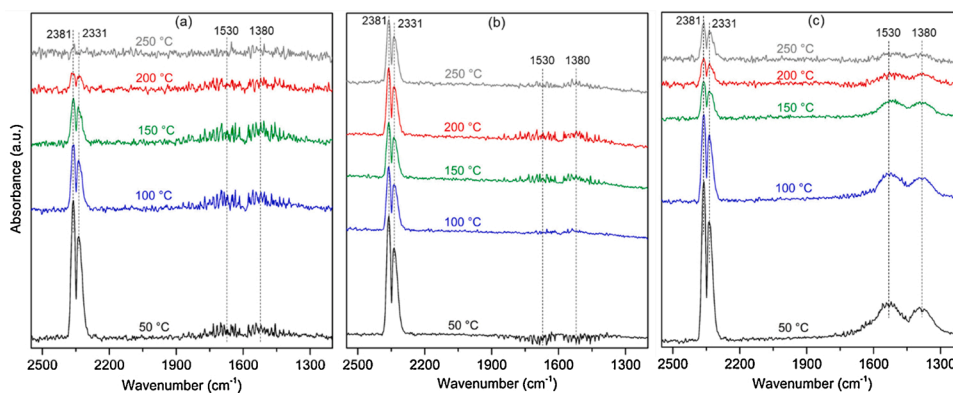
Fig. 14. In-situ DRIFTS collected during CO_2 temperature programmed desorption performed on (a) as- calcined LSNF, (b) La_2NiO_4 and (c) LSNF treated with 5 % H_2/N_2 at 800 °C for 2 h.

metal ions into the perovskite structure is faster than reduction and exsolution of the ions out from the bulk structure. LSNF sample was also treated under a redox mixture of 3 % CO + 3 % CO_2 / He at 800 °C, and the XRD of this sample is compared to that of the 5-h H_2-treated sample in Fig. S7 of the supplementary information file. It is clearly seen that La_2NiO_4 and Ni formation occurs on parent LSNF perovskite under such redox environment.

3.5. CO_2 temperature-programmed desorption DRIFTS

LSNF after reduction at 800 °C for 2 h forms an RP phase, metallic nanoparticles, and oxygen vacancies. These additional phases can affect the adsorption-desorption behavior of the catalyst, and it is important to understand the relative contribution of the individual phases. For studying the adsorption-desorption performances, CO_2 temperature-programmed desorption DRIFTS was carried out on LSNF, La_2NiO_4 and reduced LSNF samples. The La_2NiO_4 sample was chosen for the TPD test so that its effect on the adsorption-desorption behavior of the reduced LSNF can be decoupled qualitatively from the effect of oxygen vacancies and metallic nanoparticles. CO_2 was adsorbed at 50 °C, then allowed to desorb as a function of temperature. DRIFTS spectra were collected at 50 °C, 100 °C, 150 °C, 200 °C, and 250 °C during desorption from LSNF, La_2NiO_4 and reduced LSNF are shown in Fig. 14(a), (b) and (c), respectively. The bands at 2381 cm^{-1} and 2331 cm^{-1} are due to molecularly adsorbed CO_2, and those at 1530 cm^{-1} and 1380 cm^{-1} are due to chemisorbed carbonate species [36,52,53]. These carbonates act as intermediates during the CO_2 electrolysis process. DRIFTS of LSNF shows only the molecularly adsorbed CO_2, which desorbs completely at 250 °C. Presence of carbonates was not detectable with the obtained signal to noise ratio. DRIFTS of La_2NiO_4 also shows only the molecularly adsorbed CO_2, however, these physisorbed CO_2 species are still present at 250 °C, indicating a stronger adsorption of CO_2 on the RP phase oxide than on LSNF. DRIFTS of reduced LSNF shows both molecularly adsorbed CO_2 and chemisorbed carbonate species, and both of these species are present up to 250 °C. This shows better adsorption of CO_2 is facilitated on the reduced LSNF sample than on the LSNF or La_2NiO_4 samples. This also proves that the improvement in CO_2 adsorption occurring in the reduced LSNF powder is not entirely brought about by the in-situ formed RP phase, as the La_2NiO_4 sample did not show the formation of the carbonate species. Since the reduced LSNF also contains the exsoluted metal nanoparticles and a higher number of oxygen vacancies than LSNF, it can be inferred that the carbonate species seen following adsorption of CO_2 is a result of the presence of such nanoparticles and oxygen vacant sites. This experimental observation agrees well with the study by Ye et al. [54], who have shown by DFT calculations that metallic nanoparticles in conjunction with a nearby oxygen vacancy act as excellent adsorption site for CO_2 during electrolysis.
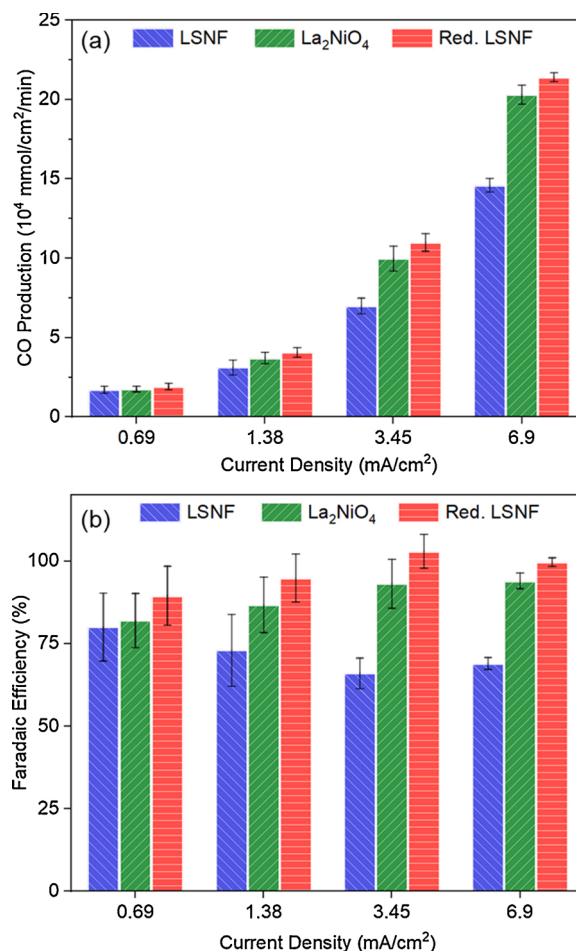

Fig. 15. (a) CO production rates and (b) corresponding Faradaic efficiencies during electrolysis of CO_2 at 800 °C at different current densities.

3.6. Electrocatalytic activity for CO_2 reduction

Fig. 15 shows the rate of CO formation normalized over the electrode geometric area when a 10 sccm stream of 40 % CO_2/He was electrolyzed over LSNF, La_2NiO_4 and reduced LSNF cathodes, at various current densities and at an operating temperature of 800 °C. Once again, the La_2NiO_4 sample is used here as a cathode so that its relative contribution towards the activity of reduced LSNF can be compared to the contribution from exsolved nanoparticles and oxygen vacancies. The corresponding Faradaic efficiencies are shown in Fig. 15(b). The LSNF
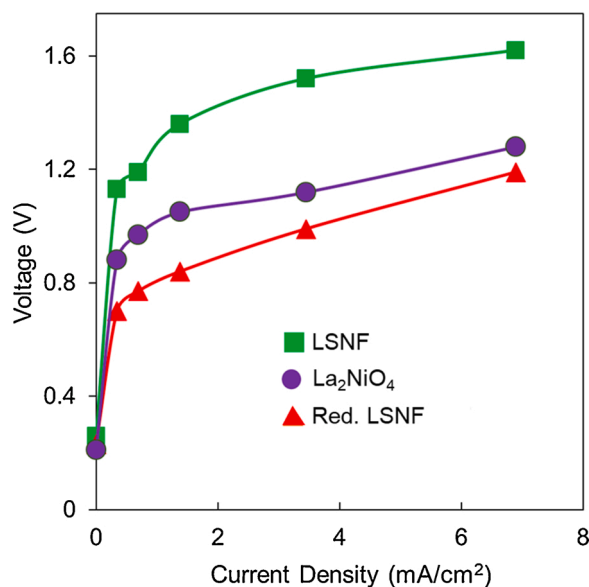
Fig. 16. Current-voltage relationship of the electrolysis cells during CO_2 electrolysis at 800 °C.

cathode showed the lowest electrochemical activity for CO_2 reduction, with the Faradaic efficiencies ranging from 65 % to 80 %. This lower Faradaic efficiency could be a result of the activation of cathode material via reduction of the B-site ion which consumes part of the supplied electrons. La_2NiO_4 cathode shows a higher Faradaic efficiency for CO production than the LSNF cathode. To form the LSNF cathode decorated with in-situ exsolved metal nanoparticles and RP phase, 5% H_2/N_2 was introduced into an LSNF cathode chamber to treat the cathode at 800 °C for 2 h. This was followed by helium purge of the chamber to flush out the residual hydrogen, and then the reactant stream of 40 % CO_2/ He was introduced. The CO formation rate obtained from this reduced cathode was found to be much higher than that shown by the LSNF or the La_2NiO_4 cathode. Faradaic efficiency for CO production between 90%–100% was obtained from the reduced LSNF cathode. One can argue that the significant improvement seen in the CO production after the LSNF cathode was exerted to exsolution environment could not be brought about by the RP phase alone, because even though the La_2NiO_4 cathode showed better activity than the LSNF cathode, the difference in CO production in that case is comparatively lower. For example, the Faradaic efficiency for CO production at 3.45 mA/cm^2 was found to be 65 %, 90 % and 100 % for LSNF, La_2NiO_4 and exsoluted LSNF, respectively. Therefore, the additional enhancement in the activity must be a result of the formation of metal nanoparticles and oxygen vacancies on the surface of the electrode. Such exsoluted phases are expected to be present during CO_2 electrolysis, as they were observed on LSNF under

CO/CO_2 redox environment (Fig. S7). There are multiple ways these nanoparticles and oxygen vacancies can enhance the CO_2 reduction activity of parent LSNF. First, due to the higher oxygen vacancy concentration, the reduced LSNF has higher ionic conductivity, which speeds up the transport of oxide ions formed by CO_2 electrolysis to the cathode-electrolyte interface [55]. Second, the surface oxygen vacancies can act as adsorption sites for CO2. Especially, CO2 adsorption on an oxygen vacancy next to a nanoparticle has been shown to be highly favorable [54]. Third, the interface between the metallic or alloy Ni-Fe particles and the perovskite shows excellent CO2 adsorption capacity [56,57]. In the current study, the perovskite at this interface is mainly of tetragonal structure. Because of such synergistic effect between the nanoparticles, oxygen vacancies and perovskite surface, the reduced LSNF adsorbs more CO_2 than the parent perovskite, which has also been shown by DRIFTS results. Moreover, the nanoparticles being metallic in nature have very high electronic conductivity. This leads to a fast charge transfer to the CO_2 adsorbed on the nanoparticle-perovskite interface, thereby improving the electrolysis kinetics.

Exsolution process not only increases the CO_2 reduction activity of the LSNF cathode but also improves the electrical energy needed for the process. Fig. 16 shows the current-voltage relationship collected from the cells during CO_2 electrolysis at 800 °C. The voltages were the highest for the cells with LSNF cathode, followed by that containing La_2NiO_4 cathode, while the cell with the reduced LSNF cathode showed the least voltage. Fig. 17 shows the electrochemical impedance spectra collected during CO_2 electrolysis on the three different cathodes at different electrolysis current densities. The impedance was observed to be the largest for the cell with LSNF cathode, while it was the lowest for the cell with reduced LSNF cathode. The high electronic conductivity of the metal nanoparticles, high ionic conductivity induced by oxygen vacancy formation, and the better adsorption of the reactant molecule CO_2 on the surface of reduced LSNF lead to the observed lower impedance of the cell. From the CO production rates, cell voltage and EIS data, it can be concluded that the increase in electrocatalytic activity is mainly brought about by the metal nanoparticles and oxygen vacancies, while the presence of the RP phase helps the cause by a smaller margin.

4. Conclusion

In summary, the present study investigated the reversible exsolution of B-site metal ions from a Ni-doped $La_{0.7}Sr_{0.2}Ni_{0.2}Fe_{0.8}O_3$ perovskite cathode under H_2 using in-situ XRD and environmental TEM techniques. The exsolution process caused the growth of Ni-rich Ni-Fe alloy nanoparticles with sizes between 1 nm–15 nm on the perovskite surface with the concomitant formation of oxygen vacancies and a Ruddlesden-Popper oxide phase. Onset temperature for the nanoparticles was found to be as low as 400 °C, which indicates the possibility of synthesizing such highly functionalized hybrid systems at temperatures much lower than the 700 °C–900 °C range typically used at present. The parent perovskite was found to transform to a tetragonal symmetry
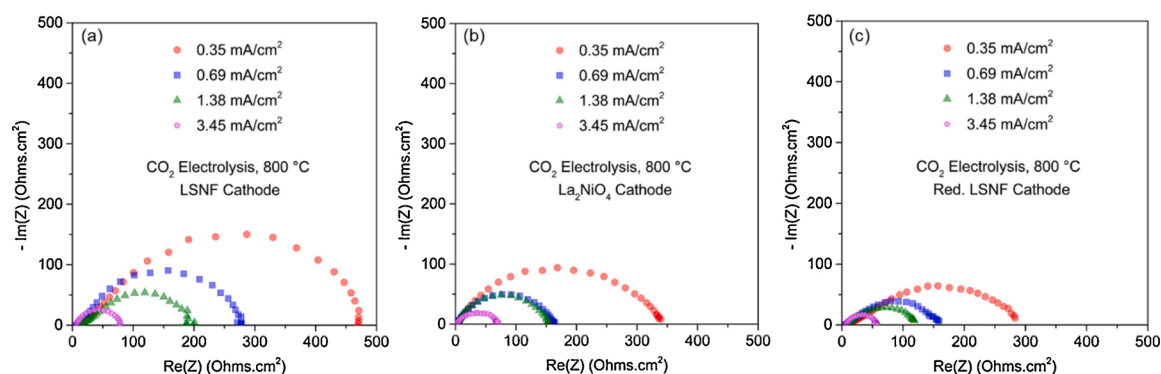

Fig. 17. EIS collected at various current densities during electrolysis of CO_2 at 800 °C.

around the nanoparticles and form a volcano-like structure so that the exsoluted nanoparticles can be socketed and stabilized in their positions, even though the lateral movement of the surface atomic layers within the nanoparticle was observed. The nanoparticle number density was found to be an order of magnitude higher than those reported for strontium titanate based exsolution systems in the literature. The perovskite before and after exsolution was tested as a cathode for CO_2 reduction and it was found that while the RP phase formed during exsolution causes a marginal improvement in the adsorption of CO_2 and electrocatalytic activity of the perovskite, the oxygen vacancies and metal nanoparticles bring significant enhancements. The exsolution phenomenon was also observed under a redox environment containing CO and CO_2.

CRediT authorship contribution statement

Dhruba J. Deka: Conceptualization, Investigation, Methodology, Data curation, Formal analysis, Writing - original draft. **Jaesung Kim:** Conceptualization, Investigation, Formal analysis, Writing - review & editing. **Seval Gunduz:** Conceptualization, Investigation, Resources, Writing - review & editing. **Mimoun Aouine:** Investigation, Formal analysis, Writing - review & editing. **Jean-Marc M. Millet:** Investigation, Formal analysis, Writing - review & editing. **Anne C. Co:** Formal analysis, Writing - review & editing. **Umit S. Ozkan:** Conceptualization, Funding acquisition, Project administration, Resources, Supervision, Formal analysis, Writing - review & editing.

Declaration of Competing Interest

The authors declare that they have no known competing financial interests or personal relationships that could have appeared to influence the work reported in this paper.

Acknowledgement

Appendix A. Supplementary data

Supplementary material related to this article can be found, in the online version, at doi:https://doi.org/10.1016/j.apcatb.2021.119917.

References

[1] J. Hwang, R.R. Rao, L. Giordano, Y. Katayama, Y. Yu, Y. Shao-Horn, Perovskites in catalysis and electrocatalysis, Science 358 (2017) 751–756.

[2] H. Zhu, P. Zhang, S. Dai, Recent advances of lanthanum-based perovskite oxides for catalysis, ACS Catal. 5 (2015) 6370–6385.

[3] K. Huang, An emerging platform for electrocatalysis: perovskite exsolution, Sci. Bull. 61 (2016) 1783–1784.

[4] D. Neagu, V. Kyriakou, I.L. Roiban, M. Aouine, C. Tang, A. Caravaca, K. Kousi, I. Schreur-Piet, I.S. Metcalfe, P. Vernoux, M.C.M. van de Sanden, M.N. Tsampas, In situ observation of nanoparticle exsolution from perovskite oxides: from atomic scale mechanistic insight to nanostructure tailoring, ACS Nano 13 (2019) 12996–13005.

[5] D. Neagu, G. Tsekouras, D.N. Miller, H. Ménard, J.T. Irvine, In situ growth of nanoparticles through control of non-stoichiometry, Nat. Chem. 5 (2013) 916–923.

[6] Y. Sun, J. Li, Y. Zeng, B.S. Amirkhiz, M. Wang, Y. Behnamian, J. Luo, A-site deficient perovskite: the parent for in situ exsolution of highly active, regenerable nano-particles as SOFC anodes, J. Mater. Chem. A 3 (2015) 11048–11056.

[7] B. Hua, M. Li, Y.F. Sun, J.H. Li, J.L. Luo, Enhancing perovskite electrocatalysis of solid oxide cells through controlled exsolution of nanoparticles, ChemSusChem 10 (2017) 3333–3341.

[8] J.G. Lee, J.H. Myung, A.B. Naden, O.S. Jeon, Y.G. Shul, J.T.S. Irvine, Replacement of Ca by Ni in a perovskite titanate to yield a novel perovskite exsolution architecture for oxygen-evolution reactions, Adv. Energy Mater. 10 (2020).

[9] S.-K. Otto, K. Kousi, D. Neagu, L. Bekris, J. Janek, I.S. Metcalfe, Exsolved nickel nanoparticles acting as oxygen storage reservoirs and active sites for redox CH4 conversion, Acs Appl. Energy Mater. 2 (2019) 7288–7298.

[10] S. Joo, O. Kwon, K. Kim, S. Kim, H. Kim, J. Shin, H.Y. Jeong, S. Sengodan, J. W. Han, G. Kim, Cation-swapped homogeneous nanoparticles in perovskite oxides for high power density, Nat. Commun. 10 (2019) 697.

[11] Y.R. Jo, B. Koo, M.J. Seo, J.K. Kim, S. Lee, K. Kim, J.W. Han, W. Jung, B.J. Kim, Growth kinetics of individual Co particles ex-solved on SrTi$_{0.75}$Co$_{0.25}$O$_{3-\delta}$ polycrystalline perovskite thin films, J. Am. Chem. Soc. 141 (2019) 6690–6697.

[12] H. Han, J. Park, S.Y. Nam, K.J. Kim, G.M. Choi, S.S.P. Parkin, H.M. Jang, J.T. S. Irvine, Lattice strain-enhanced exsolution of nanoparticles in thin films, Nat. Commun. 10 (2019) 1471.

[13] H. Arandiyan, Y. Wang, J. Scott, S. Mesgari, H. Dai, R. Amal, In situ exsolution of bimetallic Rh-Ni nanoalloys: a highly efficient catalyst for CO2 methanation, ACS Appl. Mater. Interfaces 10 (2018) 16352–16357.

[14] O. Kwon, S. Sengodan, K. Kim, G. Kim, H.Y. Jeong, J. Shin, Y.W. Ju, J.W. Han, G. Kim, Exsolution trends and co-segregation aspects of self-grown catalyst nanoparticles in perovskites, Nat. Commun. 8 (2017) 15967.

[15] T. Hong, M. Zhao, K. Brinkman, F. Chen, C. Xia, Enhanced oxygen reduction activity on ruddlesden-popper phase decorated La0.8Sr0.2FeO3-delta 3D heterostructured cathode for solid oxide fuel cells, ACS Appl. Mater. Interfaces 9 (2017) 8659–8668.

[16] R. Thalinger, M. Gocyla, M. Heggen, R. Dunin-Borkowski, M. Grünbacher, M. Stöger-Pollach, D. Schmidmair, B. Klötzer, S. Penner, Ni–perovskite interaction and its structural and catalytic consequences in methane steam reforming and methanation reactions, J. Catal. 337 (2016) 26–35.

[17] Y.F. Sun, Y.Q. Zhang, J. Chen, J.H. Li, Y.T. Zhu, Y.M. Zeng, B.S. Amirkhiz, J. Li, B. Hua, J.L. Luo, New opportunity for in situ exsolution of metallic nanoparticles on perovskite parent, Nano Lett. 16 (2016) 5303–5309.

[18] G. Tsekouras, D. Neagu, J.T. Irvine, Step-change in high temperature steam electrolysis performance of perovskite oxide cathodes with exsolution of B-site dopants, Energy Environ. Sci. 6 (2013) 256–266.

[19] D. Neagu, T.S. Oh, D.N. Miller, H. Menard, S.M. Bukhari, S.R. Gamble, R.J. Gorte, J.M. Vohs, J.T.S. Irvine, Nano-socketed nickel particles with enhanced coking resistance grown in situ by redox exsolution, Nat. Commun. 6 (2015) 8120.

[20] S.P. Jiang, Nanoscale and nano-structured electrodes of solid oxide fuel cells by infiltration: advances and challenges, Int. J. Hydrogen Energy 37 (2012) 449–470.

[21] S. Kim, A. Jun, O. Kwon, J. Kim, S. Yoo, H.Y. Jeong, J. Shin, G. Kim, Nanostructured double perovskite cathode with low sintering temperature for intermediate temperature solid oxide fuel cells, ChemSusChem 8 (2015) 3153–3158.

[22] D. Papargyriou, D.N. Miller, J.T. Sirr Irvine, Exsolution of Fe–Ni alloy nanoparticles from (La,Sr)(Cr,Fe,Ni)O$_3$ perovskites as potential oxygen transport membrane catalysts for methane reforming, J. Mater. Chem. A 7 (2019) 15812–15822.

[23] J.-h. Myung, D. Neagu, D.N. Miller, J.T. Irvine, Switching on electrocatalytic activity in solid oxide cells, Nature 537 (2016) 528–531.

[24] Y. Nishihata, J. Mizuki, T. Akao, H. Tanaka, M. Uenishi, M. Kimura, T. Okamoto, N. Hamada, Self-regeneration of a Pd-perovskite catalyst for automotive emissions control, Nature 418 (2002) 164–167.

[25] H. Tanaka, M. Taniguchi, M. Uenishi, N. Kajita, I. Tan, Y. Nishihata, Ji. Mizuki, K. Narita, M. Kimura, K. Kaneko, Self-regenerating Rh-and Pt-based perovskite catalysts for automotive-emissions control, Angew. Chemie Int. Ed. 45 (2006) 5998–6002.

[26] W. Kobsiriphat, B. Madsen, Y. Wang, L. Marks, S.A. Barnett, La0. 8Sr0. 2Cr1− xRuxO3− δ–Gd0. 1Ce0. 9O1. 95 solid oxide fuel cell anodes: Ru precipitation and electrochemical performance, Solid State Ion. 180 (2009) 257–264.

[27] T. Zhu, H.E. Troiani, L.V. Mogni, M. Han, S.A. Barnett, Ni-substituted Sr(Ti,Fe)O3 SOFC anodes: achieving high performance via metal alloy nanoparticle exsolution, Joule 2 (2018) 478–496.

[28] V. Kyriakou, D. Neagu, E. Papaioannou, I. Metcalfe, M. van de Sanden, M. Tsampas, Co-electrolysis of H2O and CO2 on exsolved Ni nanoparticles for efficient syngas generation at controllable H2/CO ratios, Appl. Catal. B 258 (2019), 117950.

[29] S. Gunduz, D.J. Deka, U.S. Ozkan, Advances in High-temperature electrocatalytic reduction of CO$_2$ and H$_2$O, in: C. Song (Ed.), Advances in Catalysis, Vol. 62, Elsevier Academic Press, Cambridge, 2018, pp. 113–165.

[30] T. Wei, L. Jia, J.-L. Luo, B. Chi, J. Pu, J. Li, CO2 dry reforming of CH4 with Sr and Ni co-doped LaCrO3 perovskite catalysts, Appl. Surf. Sci. 506 (2020), 144699.

[31] K.-Y. Lai, A. Manthiram, Evolution of exsolved nanoparticles on a perovskite oxide surface during a redox process, Chem. Mater. 30 (2018) 2838–2847.

[32] X. Yang, T. Wei, B. Chi, J. Pu, J. Li, Lanthanum manganite-based perovskite as a catalyst for co-production of ethylene and hydrogen by ethane dehydrogenation, J. Catal. 377 (2019) 629–637.

[33] Y. Wang, T. Liu, M. Li, C. Xia, B. Zhou, F. Chen, Exsolved Fe–Ni nano-particles from Sr2Fe1.3Ni0.2Mo0.5O6 perovskite oxide as a cathode for solid oxide steam electrolysis cells, J. Mater. Chem. A 4 (2016) 14163–14169.

[34] T. Liu, Y. Zhao, X. Zhang, H. Zhang, G. Jiang, W. Zhao, J. Guo, F. Chen, M. Yan, Y. Zhang, Y. Wang, Robust redox-reversible perovskite type steam electrolyser electrode decorated with in situ exsolved metallic nanoparticles, J. Mater. Chem. A 8 (2020) 582–591.

[35] T. Götsch, L. Schlicker, M.F. Bekheet, A. Doran, M. Grünbacher, C. Praty, M. Tada, H. Matsui, N. Ishiguro, A. Gurlo, B. Klötzer, S. Penner, Structural investigations of

La0.6Sr0.4FeO3−δ under reducing conditions: kinetic and thermodynamic limitations for phase transformations and iron exsolution phenomena, RSC Adv. 8 (2018) 3120–3131.

[36] D.J. Deka, S. Gunduz, T. Fitzgerald, J.T. Miller, A.C. Co, U.S. Ozkan, Production of syngas with controllable H2/CO ratio by high temperature coelectrolysis of CO2 and H2O over Ni and Co- doped lanthanum strontium ferrite perovskite cathodes, Appl. Catal. B 248 (2019) 487–503.

[37] D.J. Deka, J. Kim, S. Gunduz, M. Ferree, A.C. Co, U.S. Ozkan, Temperature-induced changes in the synthesis gas composition in a high-temperature H2O and CO2 co-electrolysis system, Appl. Catal. A Gen. 602 (2020), 117697.

[38] D.J. Deka, J. Kim, S. Gunduz, D. Jain, Y. Shi, J.T. Miller, A.C. Co, U.S. Ozkan, Coke formation during high-temperature CO2 electrolysis over AFeO3 (A= La/Sr) cathode: effect of A-site metal segregation, Appl. Catal. B 283 (2021), 119642.

[39] D.J. Deka, S. Gunduz, J. Kim, T. Fitzgerald, Y. Shi, A.C. Co, U.S. Ozkan, Hydrogen production from water in a solid oxide electrolysis cell: effect of Ni doping on lanthanum strontium ferrite perovskite cathodes, Ind. Eng. Chem. Res. 58 (2019) 22497–22505.

[40] D. Dogu, K.E. Meyer, A. Fuller, S. Gunduz, D.J. Deka, N. Kramer, A.C. Co, U. S. Ozkan, Effect of lanthanum and chlorine doping on strontium titanates for the electrocatalytically-assisted oxidative dehydrogenation of ethane, Appl. Catal. B 227 (2018) 90–101.

[41] G. Yang, W. Zhou, M. Liu, Z. Shao, Enhancing electrode performance by exsolved nanoparticles: a superior cobalt-free perovskite electrocatalyst for solid oxide fuel cells, ACS Appl. Mater. Interfaces 8 (2016) 35308–35314.

[42] Y. Gao, D. Chen, M. Saccoccio, Z. Lu, F. Ciucci, From material design to mechanism study: nanoscale Ni exsolution on a highly active A-site deficient anode material for solid oxide fuel cells, Nano Energy 27 (2016) 499–508.

[43] Z. Du, H. Zhao, S. Yi, Q. Xia, Y. Gong, Y. Zhang, X. Cheng, Y. Li, L. Gu, K. Swierczek, High-performance anode material Sr2FeMo0.65Ni0.35O6-delta with in situ exsolved nanoparticle catalyst, ACS Nano 10 (2016) 8660–8669.

[44] T. Zhang, Y. Zhao, X. Zhang, H. Zhang, N. Yu, T. Liu, Y. Wang, Thermal stability of an in situ exsolved metallic nanoparticle structured perovskite type hydrogen electrode for solid oxide cells, ACS Sustain. Chem. Eng. 7 (2019) 17834–17844.

[45] Y. Gao, Z. Lu, T.L. You, J. Wang, L. Xie, J. He, F. Ciucci, Energetics of nanoparticle exsolution from perovskite oxides, J. Phys. Chem. Lett. 9 (2018) 3772–3778.

[46] P. Atkins, J. de Paula, in: W.H. Freeman (Ed.), Physical Chemistry: Thermodynamics and Kinetics, 8 ed., 2006.

[47] K. Zhu, T. Wu, M. Li, R. Lu, X. Zhu, W. Yang, Perovskites decorated with oxygen vacancies and Fe–Ni alloy nanoparticles as high-efficiency electrocatalysts for the oxygen evolution reaction, J. Mater. Chem. A 5 (2017) 19836–19845.

[48] R. Zhang, H. Alamdari, S. Kaliaguine, Fe-based perovskites substituted by copper and palladium for NO+ CO reaction, J. Catal. 242 (2006) 241–253.

[49] M.S.S. Khine, L. Chen, S. Zhang, J. Lin, Syngas production by catalytic partial oxidation of methane over (La0. 7A0. 3) BO3 (A= Ba, Ca, Mg, Sr, and B= Cr or Fe) perovskite oxides for portable fuel cell applications, Int. J. Hydrogen Energy 38 (2013) 13300–13308.

[50] R. Pereñíguez, V.M. González-DelaCruz, J.P. Holgado, A. Caballero, Synthesis and characterization of a LaNiO3 perovskite as precursor for methane reforming reactions catalysts, Appl. Catal. B 93 (2010) 346–353.

[51] C. Batiot-Dupeyrat, G. Valderrama, A. Meneses, F. Martinez, J. Barrault, J. Tatibouët, Pulse study of CO2 reforming of methane over LaNiO3, Appl. Catal. A Gen. 248 (2003) 143–151.

[52] J. Lavalley, Infrared spectrometric studies of the surface basicity of metal oxides and zeolites using adsorbed probe molecules, Catal. Today 27 (1996) 377–401.

[53] D. Dogu, S. Gunduz, K.E. Meyer, D.J. Deka, A.C. Co, U.S. Ozkan, CO2 and H2O electrolysis Using Solid Oxide Electrolyzer Cell (SOEC) with La and Cl- doped strontium titanate cathode, Catal. Letters 149 (2019) 1743–1752.

[54] L. Ye, M. Zhang, P. Huang, G. Guo, M. Hong, C. Li, J.T. Irvine, K. Xie, Enhancing CO2 electrolysis through synergistic control of non-stoichiometry and doping to tune cathode surface structures, Nat. Commun. 8 (2017) 1–10.

[55] S. Park, Y. Kim, H. Han, Y.S. Chung, W. Yoon, J. Choi, W.B. Kim, In situ exsolved Co nanoparticles on Ruddlesden-Popper material as highly active catalyst for CO2 electrolysis to CO, Appl. Catal. B 248 (2019) 147–156.

[56] H. Lv, T. Liu, X. Zhang, Y. Song, H. Matsumoto, N. Ta, C. Zeng, G. Wang, X. Bao, Atomic-Scale Insight into Exsolution of CoFe Alloy Nanoparticles in La0. 4Sr0. 6Co0. 2Fe0. 7Mo0. 1O3-δ with Efficient CO2 Electrolysis, Angew. Chemie Int. Ed. (2020).

[57] H. Lv, L. Lin, X. Zhang, Y. Song, H. Matsumoto, C. Zeng, N. Ta, W. Liu, D. Gao, G. Wang, In Situ Investigation of Reversible Exsolution/Dissolution of CoFe Alloy Nanoparticles in a Co-Doped Sr2Fe1. 5Mo0. 5O6− δ Cathode for CO2 Electrolysis, Adv. Mater. 32 (2020), 1906193.